

Effects of 1-D versus 3-D velocity models on moment tensor inversion in the Dobrá Voda area in the Little Carpathians region, Slovakia

Zuzana Jechumtálová¹ and Petr Bulant²

¹ *Institute of Geophysics, Academy of Sciences of the Czech Republic*

² *Department of Geophysics, Faculty of Mathematics and Physics, Charles University in Prague, Czech Republic*

Abstract

Retrieving the parameters of a seismic source from seismograms involves deconvolving the response of the medium from seismic records. Thus, in general, source parameters are determined from both seismograms and the Green functions describing the properties of the medium in which the earthquake focus is buried. The quality of each of these two data sets is equally significant for the successful determination of source characteristics. As a rule, both sets are subject to contamination by effects that decrease the resolution of the source parameters. Seismic records are generally contaminated by noise that appears as a spurious signal unrelated to the source. Since an improper model of the medium is quite often employed, due to poor knowledge of the seismic velocity of the area under study, and since the hypocentre may be mislocated, the Green functions are not without fault. Thus, structures not modelled by Green functions are assigned to the source, distorting the source mechanism.

To demonstrate these effects, we performed a synthetic case study by simulating seismic observations in the Dobrá Voda area of the Little Carpathians region of Slovakia. Simplified 1-D and 3-D laterally inhomogeneous structural models were constructed, and synthetic data were calculated using the 3-D model. Both models were employed during a moment tensor inversion. The synthetic data were contaminated by random noise up to 10 and 20% of the maximum signal amplitude. We compared the influence of these two effects on retrieving moment tensors, and determined that a poor structural model can be compensated for by high quality data; and that, in a similar manner, a lack of data can be compensated for by a detailed model of the medium. For examples, five local events from the Dobrá Voda area were processed.

Keywords

ray tracing, 1-D and 3-D velocity models, earthquake mechanism, amplitude inversion, Dobrá Voda earthquakes

1. Introduction and motivation

The mountain region of the Little Carpathians in western Slovakia, especially within the zone surrounding Dobrá Voda, suffers from moderate seismicity and is now one of the most seismically active zones within Slovakia. The strongest known earthquake in the Dobrá Voda area was felt on January 9, 1906 with an intensity of $I_0 = \text{VIII-IX}$, according

to the EMS98 (magnitude of $M \sim 5.7$), and was followed by an aftershock of approximately the same magnitude ($M \sim 5.1$). The historical catalogue (Kárník, 1968, 1971) reports evidence of other felt earthquakes in 1890 ($M \sim 4.5$), 1914 ($M \sim 5.1$), 1964 ($M \sim 4.2$), and 1976 ($M \sim 4.7$). The local seismic network, Malé Karpaty (MKNET) operated by ProgSeis, has instrumentally monitored seismic activity in the region since 1985. In recent years the MKNET network has been permanently upgraded and expanded, and is currently composed of 15 three-component stations deployed to ensure the best coverage of the Dobrá Voda area. Today, events with a local magnitude of approximately zero are registered. Since 2001, the MKNET has produced data suitable for moment tensor inversion (i.e. it has detected earthquakes with good coverage of focal sphere for seismic stations and with a high enough signal-to-noise ratio). During this period the number of $M \geq 1.5$ earthquakes reached forty-nine, including eight events with $M \geq 2.5$. The largest number, 15, $M \geq 1.5$ earthquakes, were recorded in 2006. The strongest earthquake, with a local magnitude of $M = 3.4$, occurred on March 13, 2006. The events were located at depths between 2 and 17 km.

The Little Carpathians are located within the transition zone between the Eastern Alps and the Western Carpathians (Figure 1). In the south-east they border the Danube Basin, characterized by thick sediments deposited on a thinned crust. The dominant brittle structures of the Dobrá Voda area are ENE–WSW trending fault zones. The Brezová fault zone forms the northern margin of the Brezová elevation, while the southern border within the Dobrá Voda depression is represented by the distinctive Dobrá Voda fault zone (e.g., Marko *et al.*, 1991).

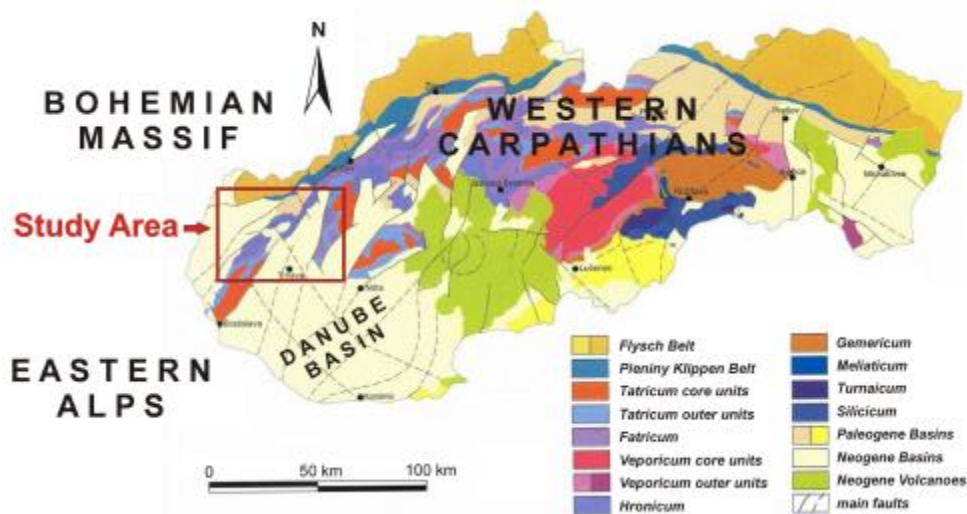


Figure 1: A schematic tectonic map of the Western Carpathians region (modified after Káčer *et al.*, 2005).

Knowledge of earthquake mechanisms within the complete moment tensor (MT) description is useful for the identification of active fault systems and for the determination of tectonic stress. Accurate moment tensor determinations are also very important for the study of non-shear faulting processes, especially for mining within a reservoir context or for volcanic areas. For such cases, the identification of real, non-shear components contained in moment tensor is necessary. Moment tensors are sensitive to the mislocation of hypocentres, to low signal-to-noise ratios, to insufficient focal

sphere coverage, and, especially, to the quality of the structural model (Jechumtálová & Šílený, 2005; Šílený, 2009; Godano *et al.*, 2011). A detailed 3-D laterally inhomogeneous model of the medium within the hypocentre area is commonly not available. Therefore, a simplified 1-D model is generally substituted. Additionally, an anisotropy is frequently present in geological structures, but is generally neglected when the source parameters are determined, resulting in the presence of spurious non-shear components within the MT (Šílený & Vavryčuk, 2002; Rössler *et al.*, 2004).

Fojtíková *et al.* (2010) studied double-couple focal mechanisms and unconstrained moment tensors of selected earthquakes occurring in the Dobrá Voda area from 2001–2009. The authors applied three methods for moment tensor inversion and compared their accuracy and stability. A 1-D structural model was employed for all three methods. For the first method, the Focmec code (Snoke, 2003) was chosen. The code inverts double-couple focal mechanisms by employing P-wave polarities. However, the Focmec code cannot be employed for studying the non-double-couple components of the moment tensor. The second method calculated the complete moment tensors from the vertical P-wave amplitudes using the AMT computer code (Vavryčuk, 2009). Of the three methods, AMT appeared to be the most reliable, but required good focal sphere coverage. Unfortunately, many events located within the Dobrá Voda area have coverage that is not sufficient. Finally, Fojtíková *et al.* (2010) performed a waveform inversion using the ISOLA computer code (Sokos & Zahradník, 2009). Contrary to AMT, ISOLA is not sensitive to focal sphere coverage and can be employed using only a few stations. On the other hand, the code is very sensitive to the structural model. To obtain reliable results, a 3-D structural model was required since a 1-D model was insufficient for the Dobrá Voda area.

Since the velocity data available for the Dobrá Voda area (Geofyzika Brno, 1985) enabled us to construct a 3-D structural model, the effects of using 1-D or 3-D models on the resulting moment tensors could be studied. In this paper, available velocity data are presented and the process of compiling the 1-D and 3-D velocity models within the area is described. To show possible distortions of the resulting moment tensors caused using a 1-D velocity model for calculating the response of the medium instead of the true 3-D model, we performed synthetic tests of the moment tensor inversion. The effect of inverting P- and S-wave amplitudes together, as compared to only inverting the P-wave amplitudes, and the influence of noise contamination in the data were also investigated. The ability to resolve the non-shear components was also analysed during the synthetic tests.

We subsequently performed a moment tensor inversion of five real earthquakes occurring in the Dobrá Voda area since 2009 that were strong enough to allow reliable determination of the source parameters. We compared the results obtained using 1-D or 3-D velocity models and concluded that the mechanisms obtained using the 3-D model were closer to pure shear-slips than the mechanisms obtained using the 1-D model.

2. The 1-D and 3-D velocity models of the Dobrá Voda area

2.1. Smoothing velocity models for ray tracing

As described above, one of the steps of the moment tensor inversion method applied was the modelling of Green functions from earthquake hypocentres to stations of the seismic network. In calculating the Green functions, the construction of a velocity model of the area was the first step. We used the ray-theory Green function in our algorithm. For this case, if discrete values of the velocity are known they should be fitted by a continuous velocity model. To perform ray tracing successfully, proper smoothing of the velocity model is key. We constructed a velocity model by fitting given values of the velocity while minimizing the Sobolev norm of the model composed of second velocity derivatives (Bulant, 2002). Velocity in the constructed model was interpolated using B-splines. The values of velocity in the prescribed spline points of the constructed model were calculated during smoothing, and were based on the given velocity data and the applied amount of smoothing.

2.2. Data for the P- and S-wave velocities, the velocity model parametrization, and the amount of smoothing

For the Dobrá Voda area, P- and S-wave velocity data were available in the form of a very sparsely sampled 3-D model created by Geofyzika Brno (1985) that consisted of $7 \times 8 \times 8$ discrete values of the P- and S-wave velocities. The data grid was rectangular but irregular, namely in the vertical direction where six levels of 7×8 grid points were available for depths from 0 to 4.8 km, with the two remaining levels of grid points located at depths of 25 and 50 km. The values at depths of 0 to 4.8 km displayed lateral variation of the velocity, whereas the velocity at the remaining two depths was laterally invariant, see Figure 2. Vertically, the data consisted of two very different parts, the upper densely sampled part with a strong velocity gradient and strong lateral variation and the lower sparsely sampled part with a weak gradient.

Slowness in the velocity model was interpolated by B-splines. As an input for velocity smoothing, parameterization of the velocity model, i.e. the number and depths of the spline points, must be manually specified. Values of velocity at the prescribed spline points were calculated during smoothing based on the velocities at the data points and on the applied amount of smoothing. The objective function y was defined as follows:

$$y = \sum_a \left[\tilde{u}(x^a) - u^a \right]^2 \left[\Delta u^a \right]^{-2} + SOBMUL^2((\tilde{u}, \tilde{u})), \quad (1)$$

where $\tilde{u}(x)$ indicates the model being constructed and Δu^a is the standard deviation of value u^a at point $x = x^a$ (Bulant, 2002). The amount of smoothing is controlled by a numerical multiplicative parameter that we call SOBMUL, an acronym for the MULtiplication of the SOBOlev norm $((\tilde{u}, \tilde{u}))$ of the model. This free parameter of the objective function was also manually prescribed. To keep the objective function unitless, the units of SOBMUL are opposite those of the Sobolev norm.

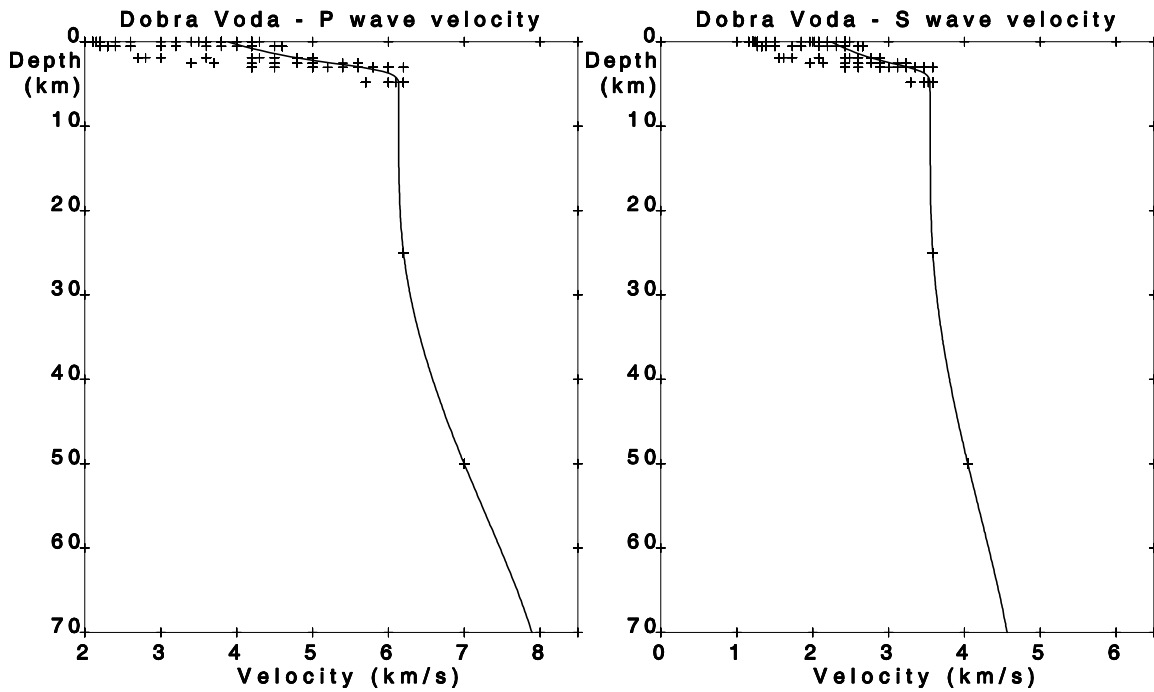


Figure 2: 1-D P-wave (left plot) and S-wave (right plot) velocity models of the Dobrá Voda area. The vertical axis indicates the depth, and the horizontal axis indicates the P-wave or S-wave velocity. Crosses indicate the value of the velocity at the 3-D data grid. The solid line shows the velocity within the constructed smooth 1-D velocity models.

2.3. The 1-D model of the Dobrá Voda area

In 1-D, the exact solution of simultaneous least-squares fitting of discrete data and the minimization of the square of the Sobolev norm composed of second derivatives yields natural cubic splines with a spline grid equal to the data grid. Consequently, we chose the 1-D velocity model parameterized using eight spline points located at the same depths as those of the data points (i.e. at depths of 0.0, 0.5, 1.9, 2.5, 3.0, 4.8, 25.0, and 50.0 km). We then performed an inversion with various amounts of smoothing beginning with minimum smoothing and gradually increasing the amount of smoothing by increasing the parameter referred to as SOBMUL. The resulting P-wave velocity models are shown in Figure 3.

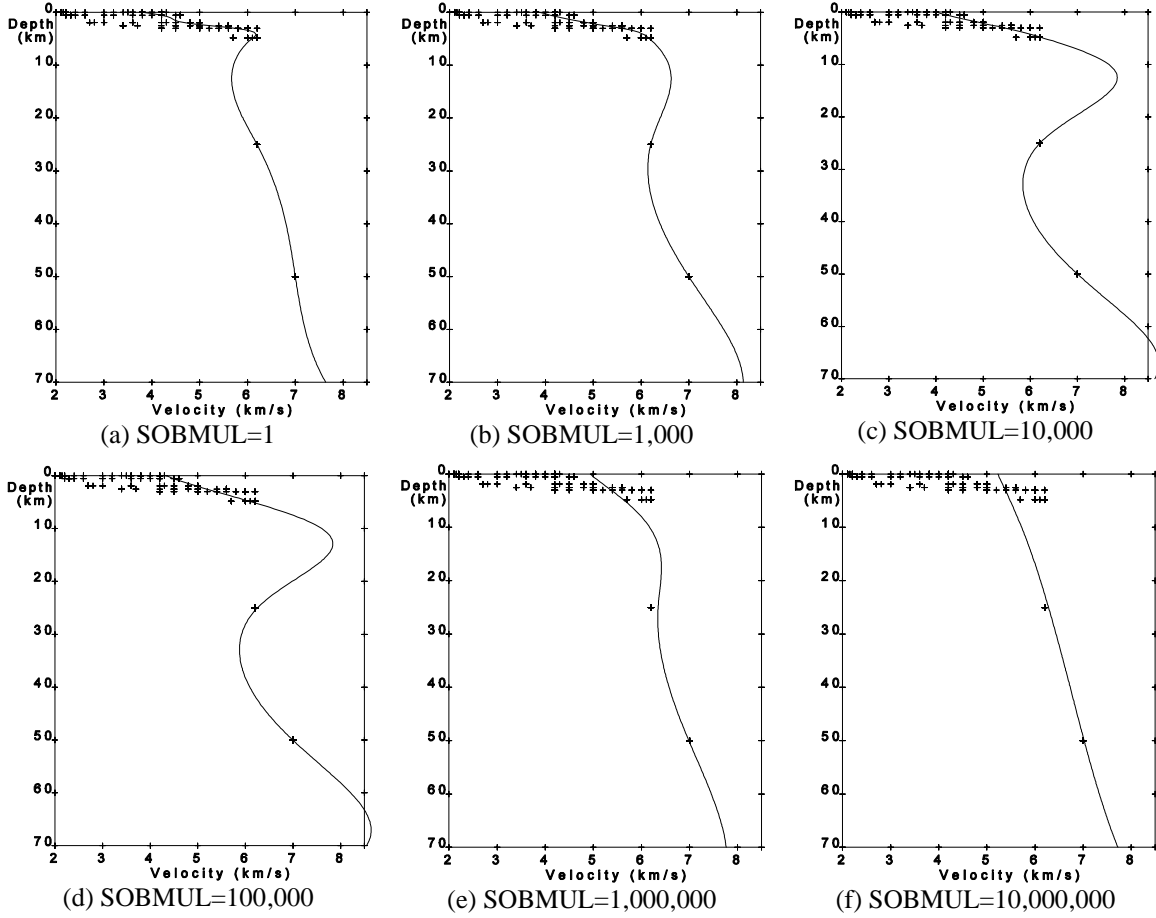


Figure 3: The 1-D P-wave velocity models obtained for various amounts of smoothing. The vertical axis indicates the depth, and the horizontal axis indicates the P-wave velocity. Crosses provide the values of the velocity of the data points. The solid line indicates the velocity in 1-D velocity models. The amount of smoothing applied ranged from $\text{SOBMUL}=1 \text{ km}^3\text{s}^{-1}$ to $\text{SOBMUL}=10,000,000 \text{ km}^3\text{s}^{-1}$. At depths of 0 to 5 km, the velocity model approximately fit the data for lower values of SOBMUL, and considerably diverged from the data for values of SOBMUL larger than $100,000 \text{ km}^3\text{s}^{-1}$. At depths of approximately 12 km, we observed the development of a low-velocity channel for $\text{SOBMUL}=1 \text{ km}^3\text{s}^{-1}$ and the development of a high-velocity channel for SOBMUL from $1,000 \text{ km}^3\text{s}^{-1}$ to $100,000 \text{ km}^3\text{s}^{-1}$. At depths of approximately 30 km, we observed the development of a low-velocity channel for SOBMUL from $1,000 \text{ km}^3\text{s}^{-1}$ to $100,000 \text{ km}^3\text{s}^{-1}$. The high- and low-velocity channels disappeared for values of SOBMUL higher than $1,000,000 \text{ km}^3\text{s}^{-1}$. From these observations we concluded that an optimum value of smoothing must be sought between $\text{SOBMUL} = 1 \text{ km}^3\text{s}^{-1}$ and $\text{SOBMUL} = 1,000 \text{ km}^3\text{s}^{-1}$.

Our aim was obtaining a velocity model that reasonably fit the data within the upper part of the velocity model at depths of 0 to 5 km, and whose lower part followed the low-velocity gradient suggested by two data points available at depths of 25 and 50 km. In Figure 3, one can see that with increasing SOBMUL the velocity model rapidly changed from a velocity model with a low-velocity channel at depths of approximately 12 km to velocity models with a high-velocity channel at these depths, and that the smooth velocity models obtained using the high SOBMUL did not sufficiently fit the data. Therefore, we sought an optimum value of smoothing in the range between $\text{SOBMUL}=1 \text{ km}^3\text{s}^{-1}$ and $\text{SOBMUL}=1,000 \text{ km}^3\text{s}^{-1}$.

Let us note that such behaviour differed from our previous experience with smoothing. For example, the behaviour differed from that experienced when smoothing the velocity models Marmoussi, Hess, or the SEG/EAGE Salt Model (Bulant 2002, 2004; Žáček 2002). For lower values of SOBMUL, these velocity models were insufficiently smooth and fit the data well. The models were reasonably smooth and reasonably fit the data for optimal SOBMUL, and were even smoother and slowly diverging from the data for higher values of SOBMUL. In other words, when we increased SOBMUL the models first became smooth and reasonably fit the data. Only after a further increase of SOBMUL did they become very smooth and begin to diverge from the data. As the velocity model for the Dobrá Voda area shown in Figure 3 (e) was quite stable and smooth, had we accepted the divergence of the velocity model from the data in the shallow part of the velocity model, we would have likely chosen a value of SOBMUL of approximately $1,000,000 \text{ km}^3 \text{ s}^{-1}$. However, since we considered this divergence to be too high, we looked for an optimal SOBMUL within the range mentioned above.

The velocity models obtained for the five values of SOBMUL within the above mentioned range are shown in Figure 4. As indicated by Figure 4, the range of optimal values of SOBMUL was quite narrow. Since the available data indicated that neither a low- nor high-velocity channel was present at depths between 5 and 25 km, we considered a value of $350 \text{ km}^3 \text{ s}^{-1}$ as an optimal value of SOBMUL.

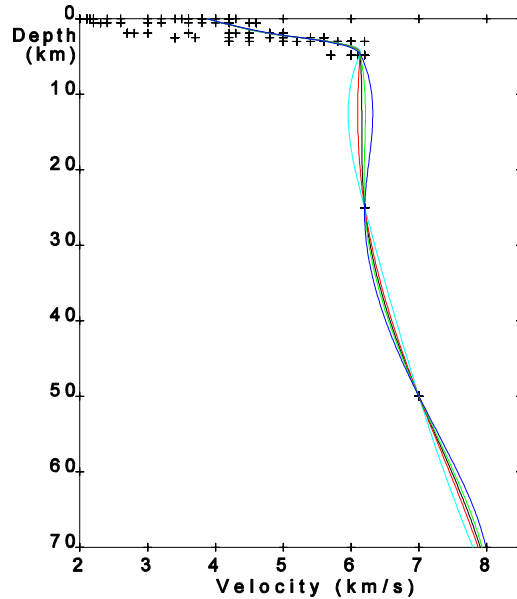
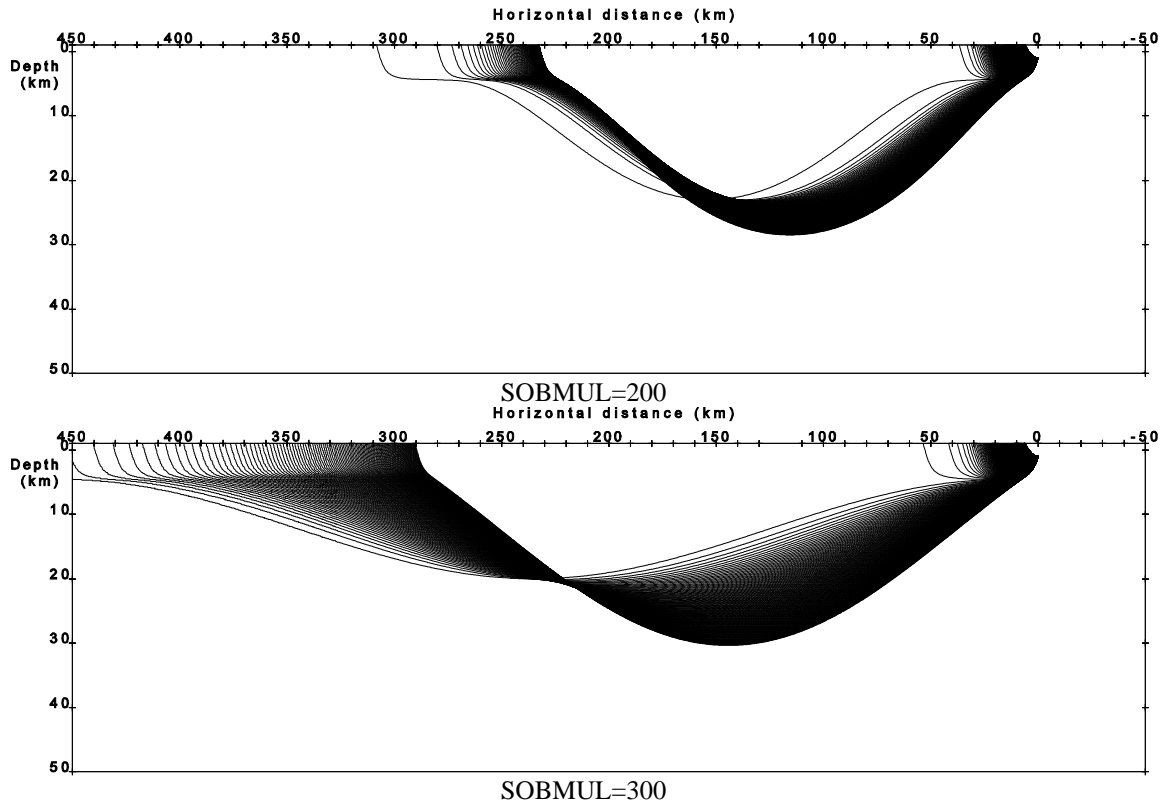


Figure 4: The 1-D P-wave velocity models obtained for values of $\text{SOBMUL}=200 \text{ km}^3 \text{ s}^{-1}$ (cyan), $\text{SOBMUL}=300 \text{ km}^3 \text{ s}^{-1}$ (red), $\text{SOBMUL}=350 \text{ km}^3 \text{ s}^{-1}$ (black), $\text{SOBMUL}=400 \text{ km}^3 \text{ s}^{-1}$ (green), and $\text{SOBMUL}=600 \text{ km}^3 \text{ s}^{-1}$ (blue). For the upper part of the velocity model at depths of 0 to 5 km the velocity remained almost unchanged. In the lower part of the velocity model, at depths of roughly 12 km, a quick change from a low-velocity channel for SOBMUL less than $350 \text{ km}^3 \text{ s}^{-1}$ to a high-velocity channel for SOBMUL higher than $350 \text{ km}^3 \text{ s}^{-1}$ was observed.

Once we chose an optimal 1-D P-wave velocity model, we checked the model using ray tracing. Figure 5 provides examples of initial-value ray tracing within the 1-D P-wave velocity models displayed in Figure 4. A low-velocity channel at depths below 5 km within the two velocity models obtained with SOBMUL lower than $350 \text{ km}^3 \text{ s}^{-1}$ caused unacceptably large geometrical spreading between the rays that emerged at the surface at distances larger than 50 km from the source. For the velocity model obtained with $\text{SOBMUL}=350 \text{ km}^3 \text{ s}^{-1}$, the velocity under 5 km was almost constant and rays emerged at the reference surface quite regularly with the maximum distance between neighbouring rays being approximately 20 km for rays emerging at the surface at distances of up to 250 km from the source. Therefore, if the distance of the rays traced with a step of 0.0002 rad was shorter than 20 km, and considering that we were able to trace rays with a step of 0.000001 rad, we estimated that it was always possible to find two-point rays (rays connecting a given source with a given receiver) that emerged less than 50 m from the receivers. Therefore, the velocity model obtained with $\text{SOBMUL}=350 \text{ km}^3 \text{ s}^{-1}$ was suitable for two-point ray tracing, although at the limit of acceptable velocity models. We were also able to determine that the high-velocity channel under 5 km within the two velocity models obtained with SOBMUL higher than $350 \text{ km}^3 \text{ s}^{-1}$ caused large geometrical spreading for rays emerging on the surface at distances larger than 250 km.

The 1-D S-wave velocity model was constructed in a similar fashion as the P-wave velocity model. Here, the reader is again referred to the right plot in Figure 2.



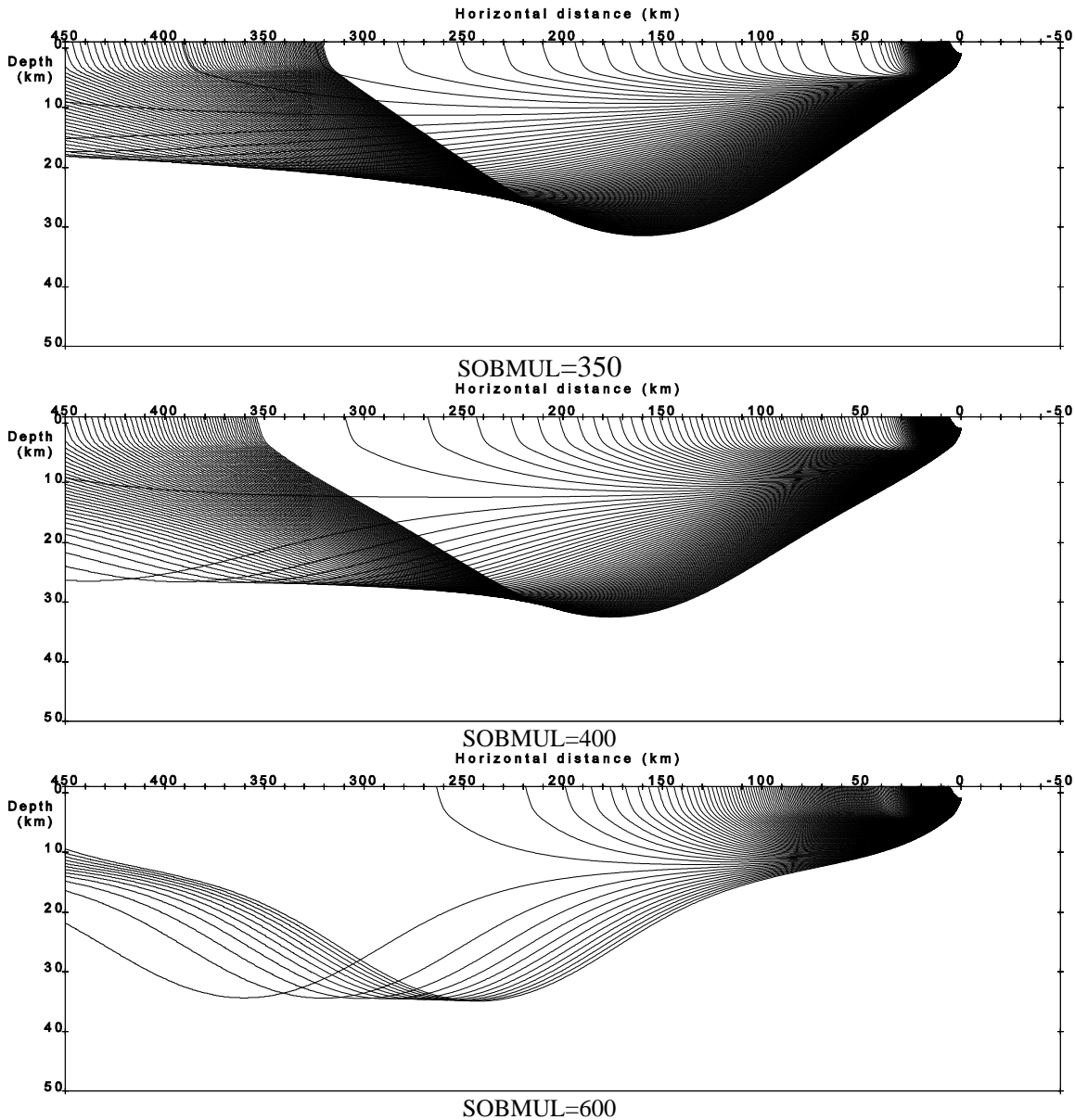


Figure 5: Rays calculated by initial-value ray tracing in the velocity models shown in Figure 4. The seismic source was located at a depth of 1 km. The first ray was shot from the source in a horizontal direction. Subsequent rays were traced with a constant step of 0.0002 rad in a vertical shooting angle. The last ray was shot under an angle of 0.82 rad from horizontal. The ratio of the horizontal to the vertical scale in the figure is 1:3.

2.4. A comparison of local 1-D velocity models

As mentioned above, data for the velocity model were available on a 3-D grid of 7 x 8 x 8 points. We viewed the data as a set of 56 vertical profiles, each consisting of eight data points, and attempted to construct 1-D velocity models for individual profiles. Figure 6 provides the constructed velocity models for two of the 56 profiles. In Figure 6, one can see that the value of SOBMUL (i.e. the amount of smoothing applied), differed considerably between the two cases. Therefore, it was obvious that finding a single value

of SOBMUL that would enable applying the smoothing algorithm with a constant smoothing weight to creating a smooth 3-D velocity model of the Dobrá Voda area was not possible.

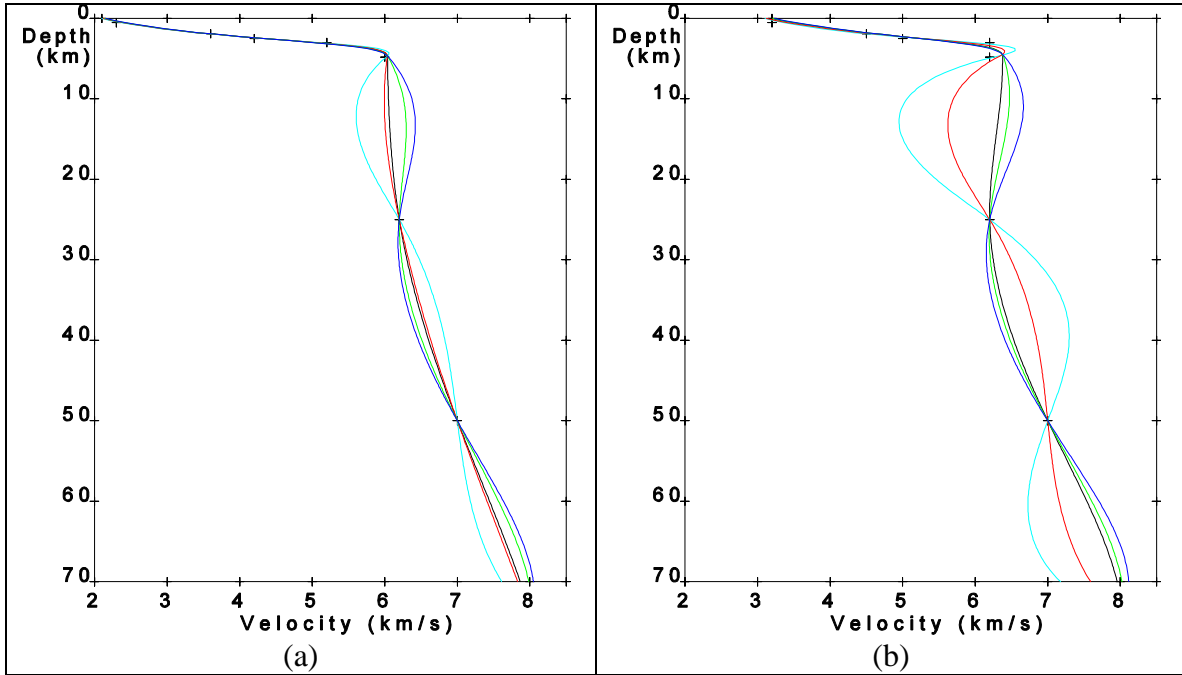


Figure 6: The 1-D velocity models obtained by an inversion of individual vertical profiles consisting of eight data points. Two of the 56 profiles obtained are shown in the figure.

In the profile shown in (a), the five velocity models correspond to the values of $\text{SOBMUL}=100 \text{ km}^3\text{s}^{-1}$ (cyan), $\text{SOBMUL}=200 \text{ km}^3\text{s}^{-1}$ (red), $\text{SOBMUL}=220 \text{ km}^3\text{s}^{-1}$ (black), $\text{SOBMUL}=300 \text{ km}^3\text{s}^{-1}$ (green), and $\text{SOBMUL}=350 \text{ km}^3\text{s}^{-1}$ (blue). An optimal model was obtained for $\text{SOBMUL}=220 \text{ km}^3\text{s}^{-1}$.

In (b), the velocity models corresponding to the values of $\text{SOBMUL}=350 \text{ km}^3\text{s}^{-1}$ (cyan), $\text{SOBMUL}=1,000 \text{ km}^3\text{s}^{-1}$ (red), $\text{SOBMUL}=2,200 \text{ km}^3\text{s}^{-1}$ (black), $\text{SOBMUL}=2,500 \text{ km}^3\text{s}^{-1}$ (green), and $\text{SOBMUL}=3,000 \text{ km}^3\text{s}^{-1}$ (blue) are shown. An optimal model was obtained for $\text{SOBMUL}=2,200 \text{ km}^3\text{s}^{-1}$.

Therefore, the optimal value of SOBMUL was ten times higher for the r.h. profile than for the l.h. profile.

2.5. A 3-D model of the Dobrá Voda area

When using the above described method of fitting the given values of velocity while minimizing the Sobolev norm of the model composed of second velocity derivatives, construction of the 3-D smooth velocity model should be, in principle, very similar to construction of the 1-D model. However, for the Dobrá Voda area, since the data consisted of two very different parts, construction of the 3-D model based solely on velocity data was impossible, mainly due to an abrupt change in the vertical velocity gradient in the data at a depth of 4.8 km combined with a lack of data at depths under 4.8 km. The lack of data caused unacceptable low- and high-velocity channels to appear at a depth of approximately 12 km.

As previously discussed in Section 3.2, the velocity channels can be eliminated by higher smoothing of the velocity models which, however, result in high deviation of the velocity models from the data for the shallow part of the models, refer to Figure 3 (e) and (f). In constructing the 1-D velocity model, we decided not to accept such a deviation of

the model from the data. For constructing the 3-D velocity model, such a high amount of smoothing was even more unacceptable since it would cause considerable distortion of the 3-D features of the data. Therefore, we needed to apply only a reasonably small amount of smoothing when constructing the 3-D velocity model. In Section 3.3, we demonstrate that individual vertical profiles required a different amount of smoothing and that the data did not allow us to apply the smoothing algorithm with a constant smoothing weight in 3-D.

One of the reasons for the above-mentioned problem was a lack of data at depths below 4.8 km. A possible solution was to complement the data using values of velocities obtained from the 1-D velocity model at depths of 5 to 45 km. Complementing the data may be justified by the fact that the original data below 4.8 km were available only at depths of 25 and 50 km and laterally invariant. Forcing the 3-D velocity model to be similar to the 1-D model below 4.8 km thus seemed reasonable.

We discretized the P-wave velocity in the 1-D model at depths of 5 to 45 km using a vertical step of 2 km, and added calculated values to the original velocity data. We then constructed the 3-D smooth velocity model using the above described method of fitting given velocity values while minimizing the Sobolev norm of the velocity model composed of second velocity derivatives. The amount of applied smoothing, described by parameter $\text{SOBMUL} = 400 \text{ km}^3 \text{ s}^{-1}$, was selected in order to avoid a velocity model that differed significantly from the data in the shallow parts, similar to construction of the 1-D velocity model. The data added for depths of 5 to 45 km stabilized the velocity model being constructed and prevented the formation of low-velocity channels for the lower values of smoothing, see Figure 7 as compared with Figures 3, 4, and 6. The suitability of the velocity model for two-point ray tracing was again checked by initial-value ray tracing, in a manner similar to the 1-D case.

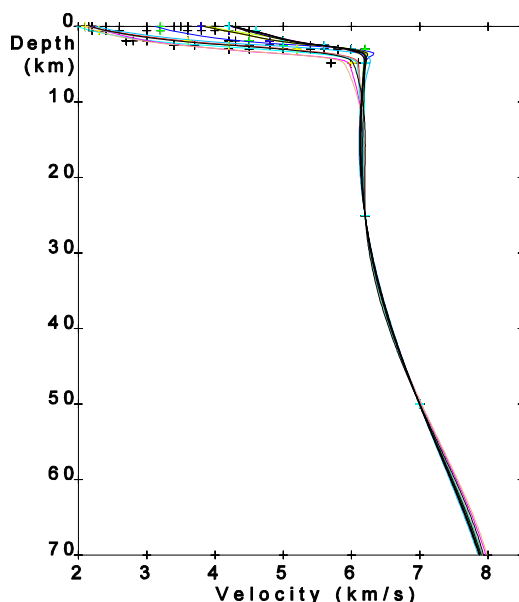
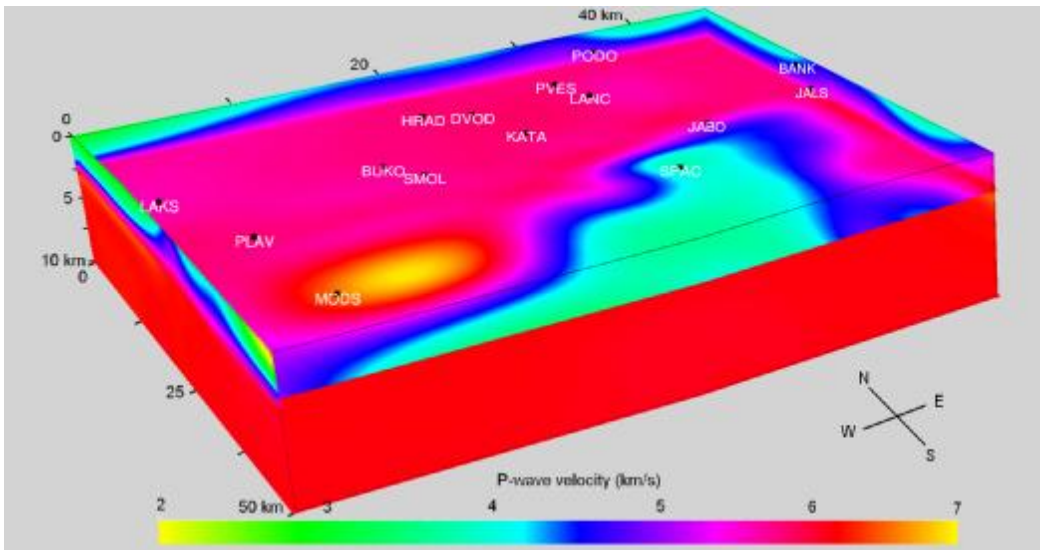
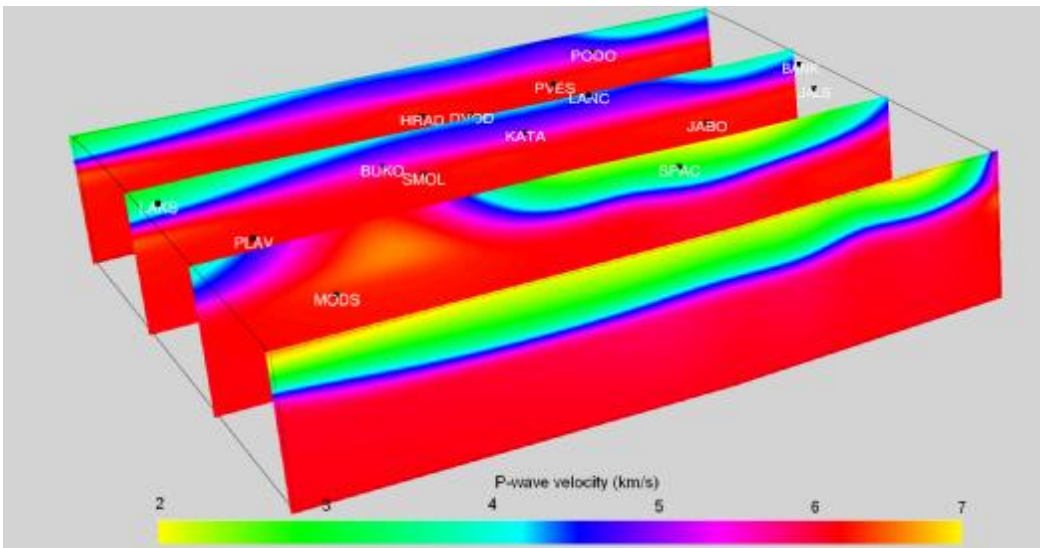


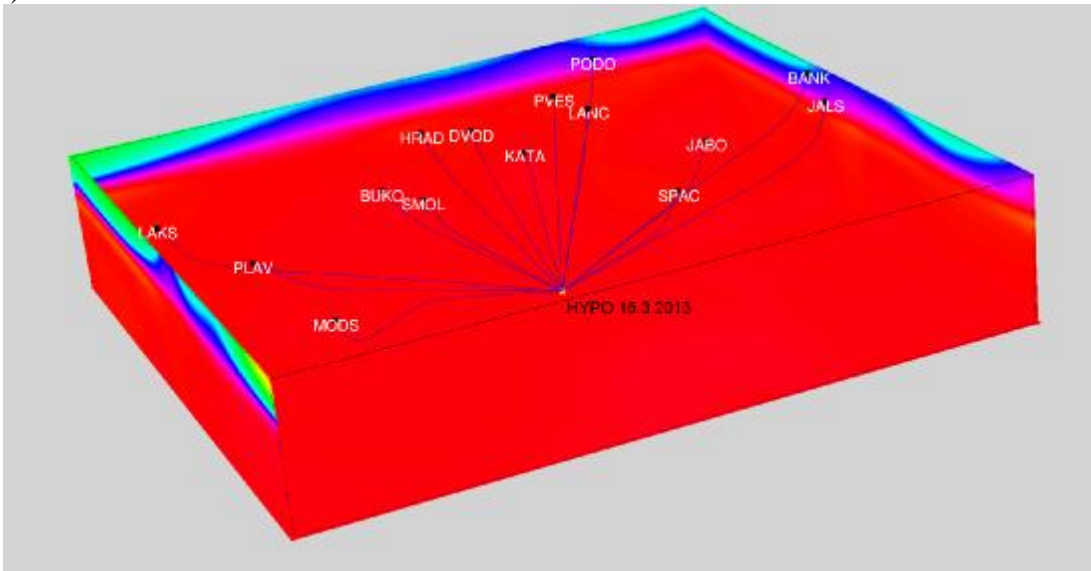
Figure 7: Vertical P-wave velocity profiles of the 3-D velocity model for Dobrá Voda are shown for comparison with Figures 3, 4, and 6. Twenty vertical profiles are shown, including the two profiles corresponding to Figure 6. In most cases, the behaviour of the velocity was reasonably smooth with no high- or low-velocity channels. The 3-D behaviour of the velocity field given by 3-D data for the first 5 km of the model continued until a depth of approximately 10 km. From this depth the model became more or less one-dimensional.



(a)



(b)



(c)

Figure 8: The upper part of the 3-D P-wave velocity model of the Dobrá Voda area from a depth of 0 to 10 km. Plot (a) provides the velocity sections for the west (left), north (back), east (right), and bottom of the velocity model together with the horizontal velocity section at a depth of 2.5 km. Plot (b) provides four vertical velocity sections through the model. Plot (c) provides the two-point rays, calculated from the hypocentre of the earthquake that occurred at 16.3.2013 at a depth of 9.8 km, to the seismic stations of network MKNET. The positions of the seismic stations are marked by black squares with the station names shown in white.

Several cross-sections of the resulting 3-D P-wave velocity model are shown in Figures 8 (a) and (b). The basic features of the area, such as higher velocities within the Little Carpathian Mountains in the SW-NE direction from station MODS to station PVES, and lower velocities within the sedimentary basin surrounding the River Váh in the area of stations SPAC and JABO, were clearly described by the model. However, artificial artefacts such as the extremely high-velocity spot close to station MODS also appeared. The two-point rays, calculated from the hypocentre corresponding to the most recent earthquake of 16.3.2013 to stations of the seismic network, are displayed in Figure 8 (c) and illustrate that the 3-D model is suitable for calculating ray-theory Green functions for the purpose of moment tensor inversion.

The 3-D S-wave velocity model was constructed analogously to construction of the 3-D P-wave velocity model, and, in general, displayed similar behaviour to the 3-D P-wave velocity model.

3. Source mechanism determinations

3.1. Methodology

The description of an earthquake mechanism using a complete moment tensor (MT) allowed us to search for general dipole sources (i.e. not only for a double couple, but also for non-shear components of the source). Moreover, MT inversion is a linear inverse problem. The MT could be retrieved from the complete waveforms (e.g., Šílený *et al.*, 1992, 1996), the amplitudes of seismic waves (e.g., Šílený & Milev, 2008), or even from their ratios (e.g., Snoke, 2003; Jechumtálová & Šílený, 2005). If the structural model does not contain sufficient detail, the waveforms may not be correctly modelled by the synthetic seismograms and the results of the waveform inversion may be significantly biased. The impact of medium uncertainty may be partly reduced using only amplitudes instead of complete waveforms, as demonstrated by Šílený & Milev (2008). Therefore, we employed an amplitude inversion. The first peak displacement amplitude of the P and S wave was estimated manually from vertical and horizontal traces of the three-component seismograms. Rarely, we observed not a single linearly polarized S wave but two linear S waves oriented perpendicular and mutually delayed. To remove shear wave splitting from the record, we merge both waves together using their vector summation (Šílený & Milev, 2008). The response of the medium to elementary dipole excitation (i.e. the Green functions) with regard to the amplitude of direct P- and S-waves was constructed with the ray method using software packages MODEL and CRT (Červený *et al.*, 1988). To solve the linear system of equations within the MT inversion, we employed the singular value decomposition method and applied the library routine from Numerical Recipes (Press *et al.*, 1992).

The complete MT is commonly split into the volumetric (V) component that can be either explosive or implosive, and the deviatoric component. Decomposition of the deviatoric component is not unique, but is traditionally split into a double-couple (DC) and a compensated linear-vector dipole (CLVD) that can either be oriented along a tension axis (T-axis) or a pressure axis (P-axis). We applied an evaluation of the percentage of individual components defined by Vavryčuk (2001).

Parallel to the MT solution, we also searched for a pure DC source. Contrary to the MT inversion, which is linear, the description of a pure DC source implies a non-linear inversion. We sought the dip, strike, and rake angles, as well as the scalar moment in a grid search using the full definition range with a step of 3° for the three orientation angles and within $(0; 2M_0)$ using a step of $0.05M_0$ as the scalar moment (where M_0 is the value determined while searching for the MT solution).

The MT solution has two more degrees of freedom than the pure DC solution, and, therefore, was a better fit for the data. The noise in the data, mismodelling of the Green functions, and other uncertainties of the MT inversion manifested themselves mainly within the non-DC part of the MT solution. Therefore, we needed to estimate the significance of the retrieved non-DC components to reveal whether or not a better match of the data for the MT model than for the DC model was not achieved by chance. We quantified the confidence of the MT model with respect to the pure DC model using an F-test by comparing the fit achieved using unconstrained MT and pure DC models. A value of 100% indicated the same confidence for the two solutions. If the probability in the F-test dropped below 50% then the MT solution was more confident than a pure DC model.

A F-test is most often employed when comparing statistical models that have been fitted to a data set using least squares in order to identify the model that best fits the data. The test is named after Sir Ronald A. Fisher who initially developed the statistic as the variance ratio. The test statistic in an F-test is the ratio of two scaled sums of the squares reflecting different sources of variability. The sums of the squares are constructed such that the statistic tends to be greater when the null hypothesis is not true. In order for the statistic to follow the F-distribution under the null hypothesis, the sums of squares should be statistically independent, and should follow a scaled chi-squared distribution. The latter condition is guaranteed if the observational errors are uncorrelated and normally distributed with a common variance. Since we inverted the amplitudes of direct P- and S-waves, not the waveforms, we did not need to take into account the data correlation as we did when inverting the filtered waveforms. The normal distribution was the issue and may be satisfied concerning ambient noise. However, errors due to hypocentre mislocation and velocity mismodelling likely violated the assumption. Therefore, applicability of the F-test was limited.

To estimate the reliability of the retrieved unconstrained moment tensors we computed confidence zones describing the distribution of the model parameters that yielded a good match to the data. The size and shape of the confidence zones told us how certain the parameters were determined. For example, if the confidence zone with a parameter was large it was poorly resolved; whereas if it was small and compact, the parameter was well constrained. We considered the confidence zone of the model parameters, \mathbf{m} , using the probability content, p , to be the set of points \mathbf{m} satisfying the following:

$$\chi^2(\mathbf{m}) < \chi_p^2 \quad (2)$$

where χ_p^2 was determined from the following condition:

$$\frac{\int_{\chi^2(\mathbf{m}) < \chi_p^2} \text{PPD} \, d\mathbf{m}}{\int_{\mathbf{m}} \text{PPD} \, d\mathbf{m}} = p \quad , \quad (3)$$

that specifies the ratio of the cumulative probability in the region to the integral of the posterior probability density (PPD) across the entire model space (Tarantola, 1987). The PPD was considered as follows:

$$\text{PPD} = \exp\left(-\frac{1}{2}\chi^2\right) \quad . \quad (4)$$

That is, having the function $\chi^2(\mathbf{m})$, we determined a particular confidence zone as the region limited by the contour χ_p^2 and possessing the probability content requested. We defined the confidence zones for the principal T, P, and N axes and for the MT decomposition in terms of the percentage of the DC, V, and CLVD components.

3.2. Synthetic tests of the moment tensor inversion

For assessing the resolution power of the monitoring network, it is reasonable to perform synthetic experiments. We designed a series of synthetic tests simulating the real configuration of the MKNET seismic network, with the aim of testing the importance of the structural model employed. The synthetic event has the same location as for the

earthquake of August 5, 2006 with a depth of 5.24 km and a local magnitude of 3.0 (Figure 9-a). Its epicentre was situated within the seismic array and therefore it has good coverage of the focal. The focal mechanism of this event (a pure double-couple source mechanism with a dip of 43° , a strike of 80° , and a rake of 10°) is displayed in Figure (9-b). For this real tectonic event the synthetic three-component P- and S-wave amplitudes were computed for the 3-D structural model. As stated previously, we used ray-theory Green functions so the P- and S-wave amplitudes were directly computed (Aki & Richards, 1980). To study the importance of the quality of the data, the amplitudes were then contaminated by artificial random white noise with a maximum amplitude equal to 10 and 20% of the respective amplitude. A total of 100 data sets were generated for each level of noise. All of the P- and S-wave amplitude datasets, the P-wave amplitude datasets, and the vertical P-wave amplitude only datasets were then inverted using the Green functions calculated using both the 3-D and 1-D structural models. We checked the resolution of the DC orientation, especially the DC/non-DC content known to be sensitive to inexact modelling of the velocity within the crust.

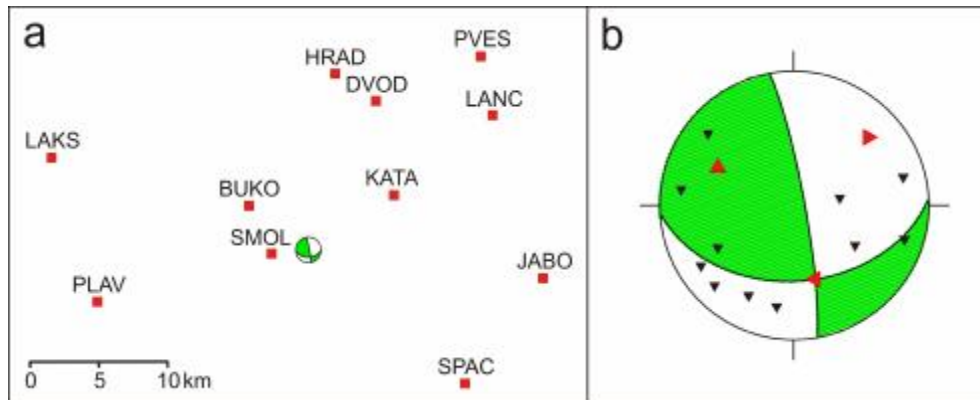


Figure 9: The source model of the tectonic event for the synthetic experiment. (a) The location of synthetic event within the MKNET seismic network; red squares – seismic stations. (b) The mechanism in the traditional fault plane solution (i.e. equal area projections of the lower hemisphere; black lines - nodal lines of the DC part; red triangle up - T axis; red triangle right - P axis; red triangle left - N axis; green zone – compressions). The projections of stations are shown as black triangles on the fault plane solution.

The results of the synthetic test, where we inverted the synthetic three-component P- and S-wave amplitudes using the Green functions computed for the 3-D and 1-D structural models (i.e. the correct and the simplified ones), are displayed in Figure 10. The moment tensors obtained by inverting the noise-free data are depicted in traditional fault plane solutions. The resultant mechanisms of noisy data were split into two separate pictures, the first for displaying the shear component and the second for displaying non-shear components. The shear part of the derived source mechanism is shown by using the principal T, P, and N axes retrieved by MT inversion. The source type plot (Hudson *et al.*, 1989) is used to distinguish the shear and non-shear components of the moment tensor. The plot, shaped like a diamond, is a two-dimensional, equal-area graphical display showing the relative position of the source mechanism to the positions of the fundamental source types. Pure-shear is located in the middle of the diamond, whereas the volumetric (V) source is displayed at the top (expansion) or bottom (implosion). Cracks, dipoles, and

the compensated linear-vector dipole (CLVD) are located on straight lines crossing the centre of the diamond.

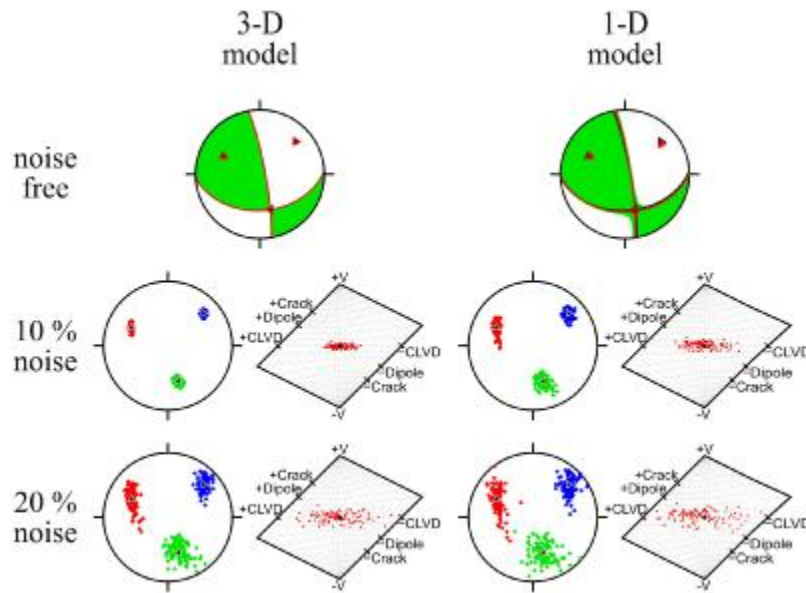


Figure 10: The synthetic experiment of the moment tensor inversion of P- together with the S-wave amplitudes using correct (3-D) and simplified (1-D) velocity models for calculation of the responses of the medium. Upper row – noise-free input data; middle row – random noise up to 10% of the maximum amplitude added to the input data; bottom row – random noise up to 20% of the maximum amplitude added to the input data. Left column – the response of the medium calculated using the 3-D velocity model; right column – the response of the medium calculated using a 1-D velocity model. The MT of noise-free data - displayed as traditional fault plane solutions; red colour – the MT solution; and black colour – the synthetic model. The MT of noisy data are displayed in the following two ways: the shear part is shown using the principal T (red), P (blue), and N (green) axes in equal-area, lower-hemisphere projections, and the non-shear part is shown using a Hudson plot, black colour – synthetic model.

Not surprising, we obtained the exact seismic source for noise-free input data when the 3-D velocity model was used to calculate the responses of the medium. For this case, we only observed the effect of the network configuration, which is very good; and, therefore, distortion of the reconstructed MTs was negligible. We would not have obtained the exact seismic source even for noise-free input data had we used the 1-D structural model. The orientation of the double-couple part of the mechanism was slightly shifted and some non-shear components appeared.

The orientation of the double-couple part of the mechanism was well retrieved only if the random noise, up to 10% of the maximum amplitude, was added; and if a 3-D structural model was used. We observed a larger uncertainty within the orientation of the T, P, and N axes for the rest of the inversions where random noise was added to the data. However, as for the DC/non-DC content of the resulting MTs, a rather large distortion appeared. Decompositions for the complete moment tensor are summarised in Table 1. The average values for each component, together with their standard deviations, are provided for noisy datasets. The components of the MT were not independent of one another, but the expression, at least, provided an estimate of the statistical scatter.

The noise was mainly converted into the CLVD component and, considerably less, into the V component. Decomposition of the moment tensor was retrieved in a more precise manner using the 3-D velocity model rather than the 1-D velocity model, implying that for the case of structural mismodelling or noisy data, the procedure creates spurious non-double-couple components of the unconstrained MT in an effort to fit the data.

	3-D model		1-D model	
noise-free	DC	100.0%	DC	94.7%
	V	0.0%	V	3.6%
	CLVD	0.0%	CLVD	1.7%
10% noise	DC	88.0±7.6%	DC	77.8±12.7%
	V	-0.7±2.7%	V	1.3±5.0%
	CLVD	-1.7±12.1%	CLVD	1.4±21.7%
20% noise	DC	70.6±18.2%	DC	64.3±19.9%
	V	0.0±7.3%	V	1.6±9.2%
	CLVD	2.6±29.1%	CLVD	6.6±33.5%

Table 1: Decomposition of the moment tensors of synthetic tests, where we inverted the three-component P- and S-wave amplitudes using the Green functions computed for 3-D and 1-D velocity models into the percentage of the double-couple (DC), the volumetric component (positive for an explosion and negative for an implosion), and the compensated linear-vector dipole (positive if oriented along the tension and negative if oriented along the pressure axis).

Inverting both the P- and S-wave amplitudes, as compared to the inversion of P-wave amplitudes only, is known to markedly improve the resolution of the mechanism’s orientation (Jechumtálová *et al.*, 2013; Šílený *et al.*, 2013). Nevertheless, the amplitudes of the S-wave are not always easily recognized because the S-wave can be covered by the P-wave coda. Therefore, we performed the same synthetic tests for P-wave amplitude datasets and vertical P-wave amplitude only datasets (the case when uniaxial sensors were employed). The amplitudes were again contaminated by artificial random white noise, with the maximum amplitude equal to 10 and 20% of the respective amplitude. A total of 100 data sets were generated for each level of noise. In total, the 10 and 20% noise contaminations of P-waves were smaller than those for the case of P- and S-waves, a consequence of the noise being constructed as a percentage of the maximum amplitude within the dataset. Since S-waves are generally stronger than P, the noise amplitudes were related to the percentage from S-waves, with the noise contamination of P-waves being larger for cases when the P- and S-waves were inverted together than if the P-waves were treated alone. The process of noise contamination indicates that the noise experiments incorporating both P- and S-waves, on the one hand, and the experiments with P-waves only, on the other hand, were not comparable.

The results of the synthetic tests where we inverted the synthetic three-component P-wave amplitudes and the vertical P-wave amplitude using only the Green functions computed for the 3-D and 1-D structural models (i.e. the correct and the simplified ones) are exhibited in Figure 11. The MTs obtained by inverting noise-free data are depicted in the traditional fault plane solutions. The resultant mechanisms of the noisy data are shown using the principal T, P, and N axes and with a Hudson plot. The decomposition

of the resulting MTs is expressed in the percentages provided in Table 2. The average values for each component together with their standard deviations are also provided for noisy datasets.

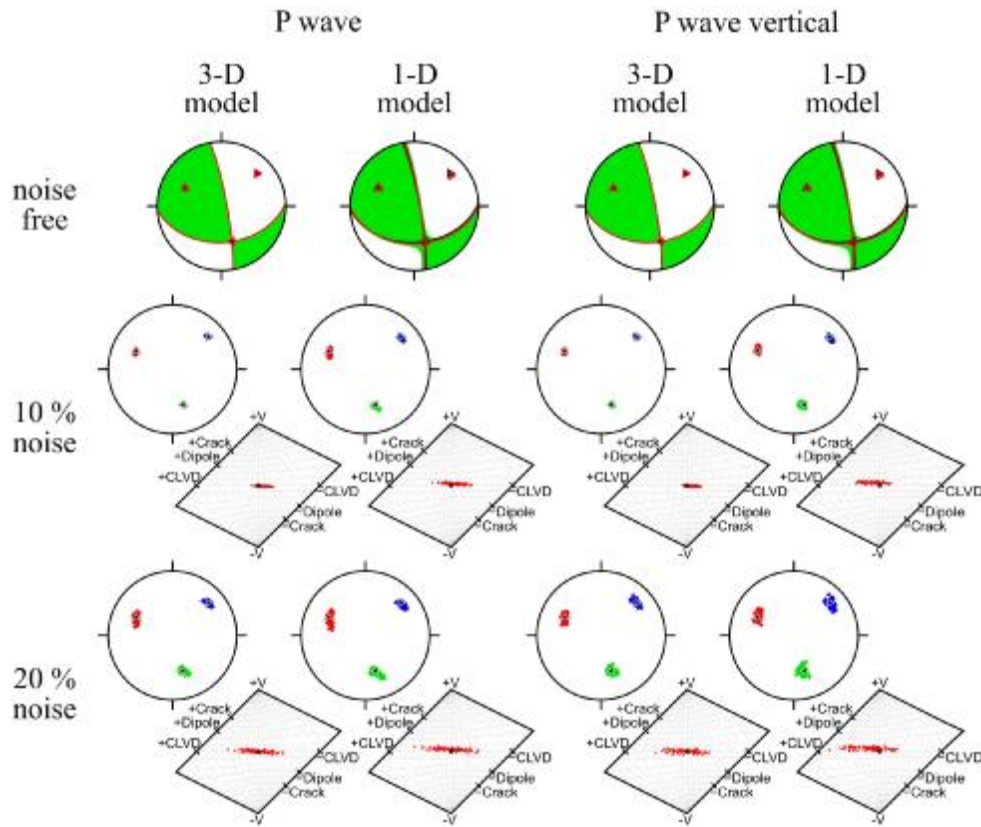


Figure 11: The synthetic experiments of moment tensor inversion for the P-wave amplitude and for the vertical P-wave amplitude obtained using correct (3-D) and simplified (1-D) velocity models for calculating the responses of the medium. Upper row – noise-free input data; middle row – random noise up to 10% of the maximum amplitude added to the input data; bottom row – random noise up to 20% of the maximum amplitude added to the input data. The columns from left to right: the inversion of the P-wave amplitude using 3-D and 1-D models, and the inversion of the vertical P-wave amplitude using 3-D and 1-D models. For details see the caption of Figure 10.

	P wave			
	3-D model		1-D model	
noise-free	DC	100.0%	DC	94.7%
	V	0.0%	V	3.6%
	CLVD	0.0%	CLVD	1.7%
10% noise	DC	90.1±6.2%	DC	86.9±7.5%
	V	-1.5±0.8%	V	2.5±1.4%
	CLVD	-7.7±6.7%	CLVD	-4.8±12.2%
20% noise	DC	84.4±10.7%	DC	79.5±12.7%
	V	0.2±2.0%	V	3.6±2.3%
	CLVD	0.9±17.3%	CLVD	2.4±20.7%

Table 2: Decomposition of the moment tensors of synthetic tests, where the P- wave amplitudes and the vertical P-wave amplitudes were inverted using the Green functions computed for the 3-D and 1-D velocity models, for the percentage of the double-couple (DC), for the volumetric component (positive for an explosion and negative for an implosion), and the compensated linear-vector dipole (positive if oriented along the tension and negative if oriented along the pressure axis).

The results are very similar to the previous case. For noise-free input data, we obtained the exact seismic source when the 3-D velocity model was used to calculate the responses of the medium, but a slightly inexact source (more than 5% of the non-shear component appeared) when we used the 1-D velocity model.

The effect of noise contamination had a character similar to that when the P- and S-wave amplitudes were inverted. The noise was largely converted into the CLVD component and, considerably less, into the V component. However, the ratio between the CLVD and V components was even higher. No large differences between the inversion of the three-component P-wave amplitudes and the vertical P-wave only amplitudes were determined. Decomposition of the moment tensor could be retrieved more precisely using the 3-D velocity model as compared to the 1-D velocity model. We also performed a synthetic test using a non-shear source. The deviations between synthetic and retrieved source parameters were very similar.

Synthetic experiments with correct and simplified velocity models demonstrated that the more exact the structural model, the more accurate the results obtained. Thus, we could determine reliable source parameters even for smaller events if we were able to construct Green functions using a 3-D laterally inhomogeneous model.

3.3. Dobrá Voda sample events

During the year 2010, the MKNET network was significantly upgraded. Since that time, several microearthquakes have occurred in the mountain region of the Little Carpathians. The five strongest events (Table 3), as recorded by a number of stations, were suitable for a moment tensor inversion. We processed these five events and included into the inversion all of the stations that recorded these events, (i.e. also the stations of neighbouring networks). The seismic viewer "OP" developed for an interactive data inspection was used as the basic tool for visualizing and analysing local seismic data (Kolář, 2007). The velocity records were integrated into the displacement records, and the P- and S-wave amplitudes were measured using particle-motion diagrams.

Date	Origin time [UTC]	Latitude [°]	Longitude [°]	Depth [km]	M _L
20.7.2011	18:30:58.0	48.62	17.87	16.0	2.1
21.10.2011	15:58:39.3	48.53	17.17	8.0	2.5
5.3.2012	22:56:57.1	48.55	17.12	14.0	3.1
18.11.2012	21:23:31.0	48.58	17.61	5.2	1.9
16.3.2013	09:38:38.9	48.54	17.57	9.8	1.5

Table 3: Events suitable for MT inversion. Data provided by ProgSeis.

The seismograms allowed reliable P- and sometimes S-wave amplitude estimations that contributed to the confidence of the reconstructed MTs demonstrated in the synthetic modelling. We inverted the ground-displacement peak amplitudes of both P- and S-waves in order to retrieve the moment tensors of selected microearthquakes together with pure DC sources (Figure 12). For each event, we inverted both the full MT model and the pure DC model using 1-D and 3-D structural models for calculating the responses of the medium. Only for the event of November 18, 2012 did the probability in the F-test drop below 50% (to exactly 31%) when using the 1-D structural model in the inversion. This result indicates that the unconstrained moment tensor satisfied the data better than a pure DC model. Nevertheless, when the 3-D velocity model was used to calculate the responses of the medium the probability in the F-test again increased up to 91%, indicating that the non-shear components were not significant even for this event and that they were caused by mismodelling. It is necessary to point out, that this event occurred at the depth of 5.2 km, and neglecting the 3-D structure in the upper 5 km of crust was not suitable. The other two events displaying differences between the 1-D and 3-D model in Figure 12 were the events of 21/10/11 and 16/03/13 located at depths of 8 and 9.8 km; the deep events of 05/03/12 and 20/07/11 located at 14 and 16 km displayed less differences between the 1-D and 3-D models. The decomposition of the MTs are presented in Table 4. The resultant MTs indicated a dominance for the DC components in almost all cases, with the non-DC part remaining low. Moreover, the value of non-DC was smaller for the inversion when the 3-D velocity model was used as compared to the 1-D model, with the effect being well pronounced especially with regard to the CLVD component. Since the sensitivity of the non-DC is related to noise contamination, mislocation, irregular focal sphere coverage, the accuracy of structural modelling, as demonstrated in the synthetic experiments, as well as the results of the F-test, the non-DC components were likely insignificant for this case.

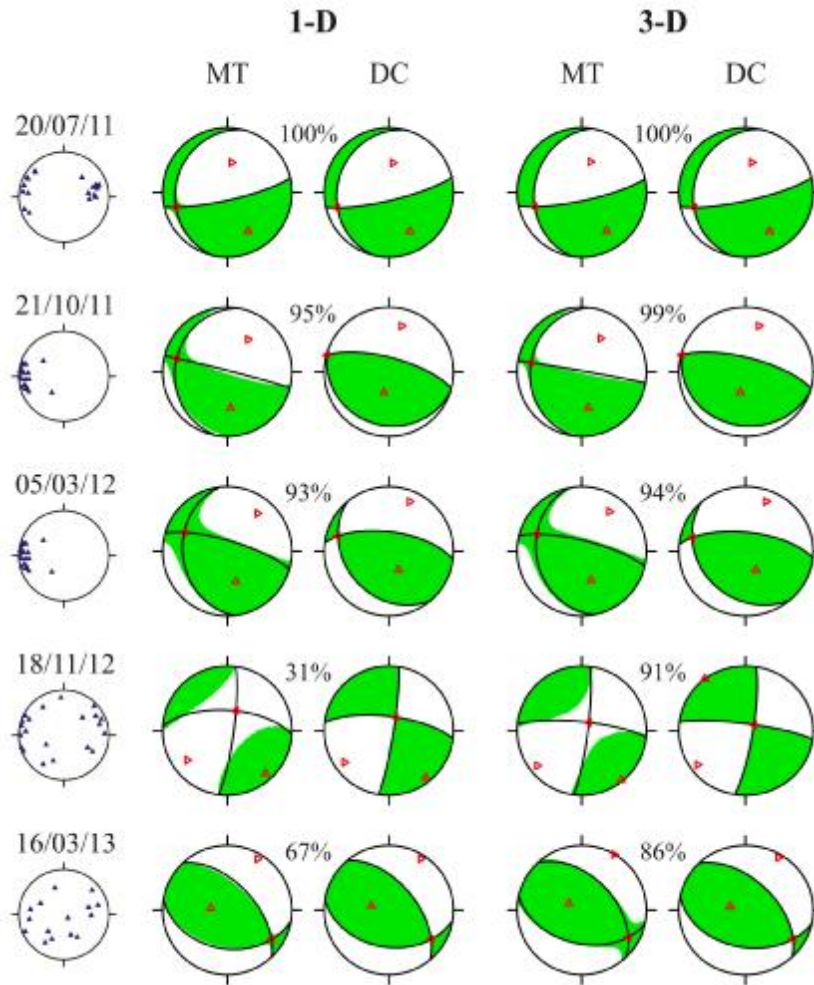


Figure 12: The full MT model and pure DC model inversions of sample events from Dobrá Voda. Leftmost column – focal sphere coverage. Left two coloured columns – the 1-D model used to calculate the responses of the medium; right two coloured columns – the 3-D model used to calculate the responses of the medium. Each row represents a different seismic event from the mountain region of the Little Carpathians. The F-test probability (as a percentage) comparing the unconstrained MT and the pure DC model is displayed for each case.

	20/07/11	21/10/11	05/03/12	18/11/12	16/03/13
1-D model	DC 95.9%	DC 64.2%	DC 75.9%	DC 23.6%	DC 77.8%
	V -0.5%	V -8.2%	V 6.2%	V -10.1%	V -6.9%
	CLVD -3.6%	CLVD -27.6%	CLVD -17.9%	CLVD 66.3%	CLVD -15.3%
3-D model	DC 99.5%	DC 75.2%	DC 86.9%	DC 59.4%	DC 88.5%
	V -0.1%	V -6.9%	V 7.1%	V -3.4%	V 2.5%
	CLVD 0.4%	CLVD -17.9%	CLVD -6.0%	CLVD 37.2%	CLVD 9.0%

Table 4: Decomposition of the moment tensors of sample events from the Dobrá Voda area to the percentage of the double-couple (DC), the volumetric component (V, positive for explosion and negative for implosion), and the compensated linear-vector dipole (CLVD which is positive if oriented along the tension and negative if oriented along the pressure axis).

Positions of the event locations and the positions of the seismic stations within the MKNET network are displayed in Figure 13, which also provides the moment tensors retrieved using the 3-D model to calculate the responses of the medium. The mechanisms retrieved were in good agreement with present-day tectonic stress within the Dobrá Voda area as determined by Fojtíková *et al.* (2010), who applied the slip shear stress component criterion within the stress inversion. Principal stresses were orientated (azimuth/plunge) as follows: $\sigma_1 = 210\text{--}220^\circ/5\text{--}25^\circ$, $\sigma_2 = 70\text{--}105^\circ/55\text{--}75^\circ$, and $\sigma_3 = 305\text{--}315^\circ/15\text{--}25^\circ$, and the shape ratio was $R=0.45\text{--}0.60$. The azimuth was measured clockwise from the north and plunged downward from the horizontal plane. The retrieved maximum compression rests along the belt of the Little Carpathians.

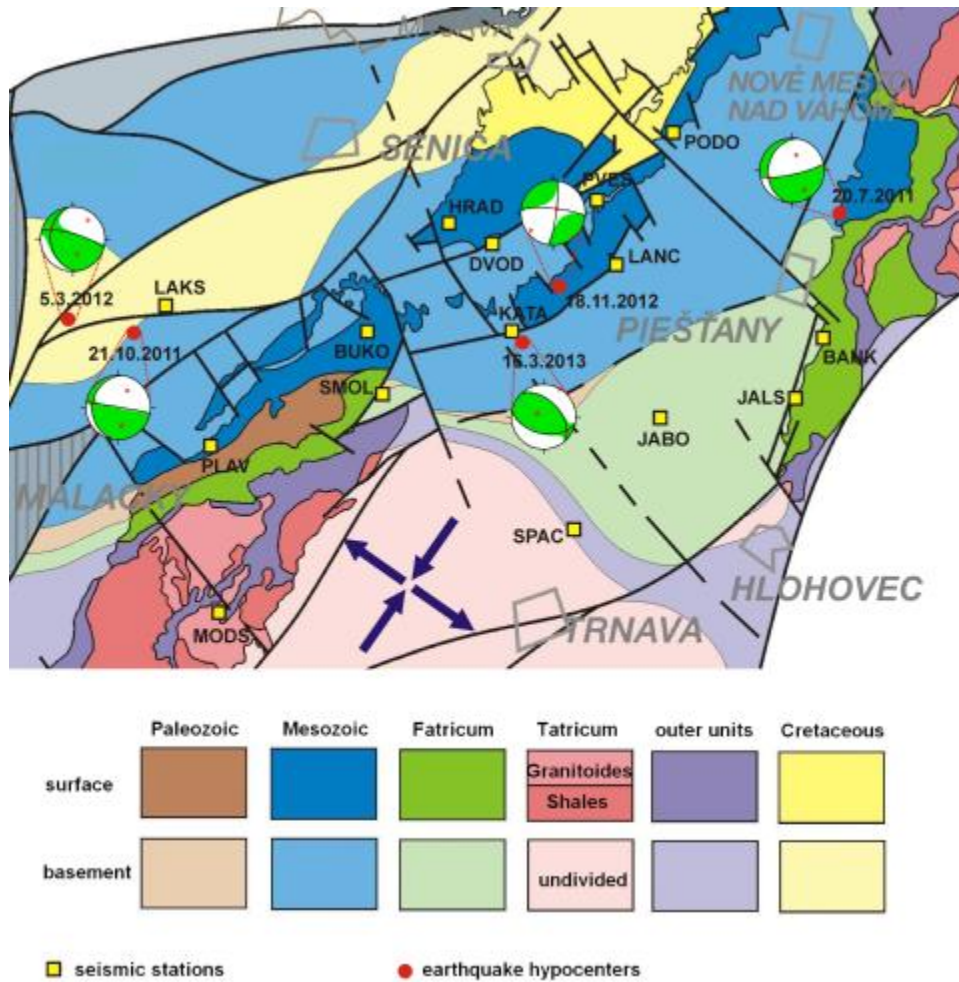


Figure 13: A schematic geological-tectonic map of pre-Tertiary bedrock within the south-west segment of the Little Carpathians (adapted from Mahel', 1986 and Hók *et al.*, 2009), with the locations of the sample events from the Dobrá Voda area (red dots) and the positions of the seismic stations of the MKNET network (yellow squares) - shown together with fault plane solutions of the full moment tensor inversions using the 3-D model to calculate medium responses. The basement geological units are covered by sediments with lower velocities. Blue arrows indicate the direction of maximum compression and maximum extension within the Dobrá Voda area according to Fojtíková *et al.* (2010).

3.4. A detailed analysis of the strongest event

A discrepancy in the depth of the strongest event on March 5, 2012 appeared. Two institutes assessed two different locations, as follows: (a) ProgSeis used records from the local MKNET seismic network and fixed its epicentre at 48.55N, 17.12E with a depth of 14 km; and (b) the Geophysical Institute of the Slovak Academy of Sciences used stations within the Slovak national network and the global structural model IASP and fixed the epicentre at 48.55N, 17.16E with a depth of 4.7 km.

To verify the probable depth of the event, we decided to compare real waveforms with the synthetic seismograms corresponding to the event located at both depths. For this test we chose the nearest station to the epicentre - Lakšár (LAKS). To calculate complete synthetic seismograms, modelling was performed using full-wave (complete) Green functions calculated using the discrete wave-number method (Coutant, 1990; Bouchon, 2003). The method required a layered velocity model of the crust. Therefore, we simplified our 1-D gradient model to seven layers (Table 5). Synthetic seismograms of strike-slip events with hypocentral depths of 4.7 and 14 km are displayed, in Figure 14, together with the ground displacement recorded at station LAKS. No filtering was used for real/synthetic waveforms. In the synthetic seismograms we observed some oscillations prior to P-wave arrival, caused by the choice of numerical method. A difference between P- and S-wave arrivals of approximately 1.6 s at station LAKS was seen on the seismograms. Synthetic tests indicated that this difference was 0.67 s for a hypocentral depth of 4.7 km, and 1.5 s for 14 km. Although a simplified velocity model was used and synthetic waveforms did not fit the real seismograms, it was clear that the location provided by ProgSeis was more probable.

Depth of layer top [km]	v_P [km/s]	v_S [km/s]	ρ [g/cm ³]	Q_P	Q_S
0	4.100	2.320	2.140	225	100
1.0	4.440	2.510	2.390	225	100
2.0	5.220	2.950	2.444	225	100
3.0	5.880	3.320	2.504	225	100
4.0	6.130	3.460	2.570	225	100
6.0	6.140	3.468	2.610	225	100
20.0	6.142	3.470	2.620	225	100

Table 5: The 1-D velocity model of the crust used for modelling full waveforms; v_P and v_S are the P- and S-wave velocities, respectively; ρ is the density; and Q_P and Q_S are the quality factors of P- and S-waves, respectively.

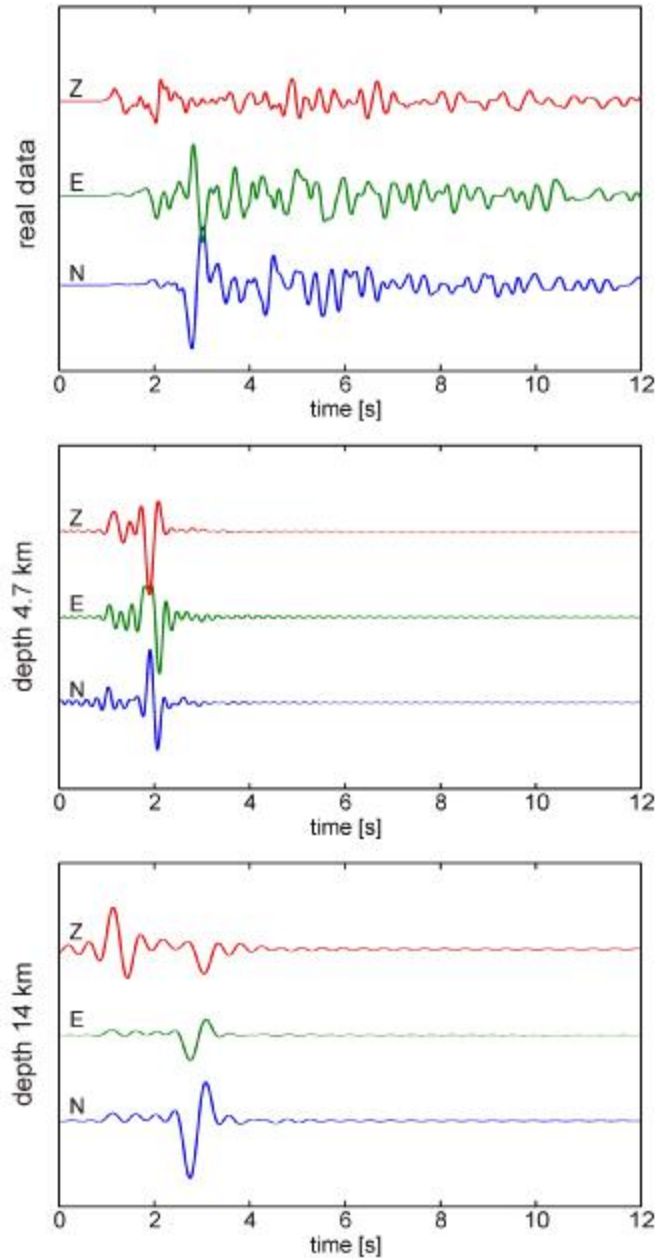


Figure 14: Example of seismograms for the event on March 5, 2012, 22:56:57.1 UTC, from the nearest station LAKS. The seismograms depicted represent (from the top panel to the bottom panel) the recorded ground displacement, synthetic seismograms for a hypocentral depth of 4.7 km, and synthetic seismograms for a hypocentral depth of 14 km.

To make sure we chose the correct location depth, we performed another test. Since the event location significantly affects the ray paths, we computed the responses of the medium using a 3-D structural model for different hypocentral depths and analysed the impact of depth variations on moment tensor solutions (Figure 15). The source mechanisms retrieved for different focal depths, the MT decomposition, and the values of the normalized root mean squares (NRMS) are presented in Table 6. The fit of the data improved with increasing focal depth. The orientation of the shear part of the MT

changed smoothly. The higher the focal depth, the higher the content of the DC included in the MT. On the basis of these results, we again determined that the ProgSeis's location was more reliable.

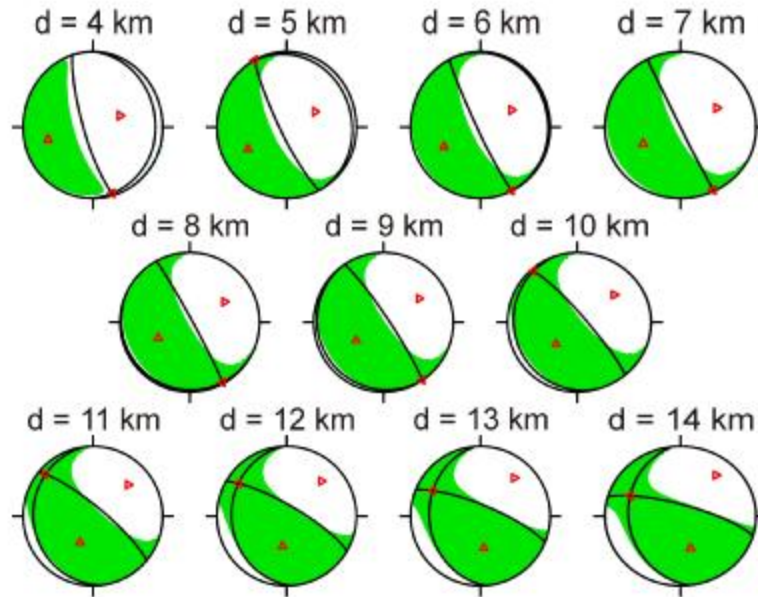


Figure 15: Source mechanisms for the actual event on March 5, 2012, retrieved using a general moment tensor and different focal depths. The traditional fault-plane solution and the principal T, P, and N axes are displayed.

depth [km]	NRMS	strike [°]	dip [°]	rake [°]	DC [%]	V [%]	CLVD [%]
4	0.398	163/1	79/11	-94/-72	42.2	-19.9	-37.9
5	0.330	153/329	82/8	-90/-93	44.7	-15.9	-39.4
6	0.284	155/336	86/4	-90/-89	52.6	-12.6	-34.8
7	0.252	154/64	90/2	-92/0	57.9	-10.0	-32.1
8	0.229	331/119	4/87	57/92	61.0	-7.5	-31.5
9	0.215	145/326	6/84	89/90	61.3	-4.8	-33.9
10	0.205	162/319	10/81	112/86	61.1	-1.9	-37.0
11	0.199	173/310	16/79	133/79	62.1	1.0	-36.9
12	0.196	177/300	22/77	145/72	66.1	3.8	-30.1
13	0.195	176/292	28/77	151/66	75.2	6.1	-18.7
14	0.194	174/286	32/77	154/61	86.9	7.1	-6.0

Table 6: Source mechanisms for the actual event on March 5, 2012, retrieved for different focal depths. The decomposition of the moment tensors of the sample events from the Dobrá Voda area to the percentage of the double-couple (DC), the volumetric component (V) and the compensated linear-vector dipole (CLVD).

We also performed a detailed error analysis of the unconstrained moment tensor inversion by constructing confidence zones for the strongest event on March 5, 2012 (Figure 16). The shape of the confidence zone provided more insight into the resolution of the source mechanism, namely on the principal axes orientation and the content of the non-shear components. We defined the confidence zones for the principal T, P and N axes (red, blue and green, respectively), which provided us with information regarding the uncertainty for a determination of the orientation. In Figure 16, these zones are presented in an equal-area, lower-hemisphere projection together with the traditional fault-plane solution. Histograms of the individual components of the decomposed MT solution, namely the double-couple (DC), volumetric (V), and compensated linear-vector dipole (CLVD) are also shown to provide information on the shear vs. non-shear content. The colour shades (dark, medium and light) represent confidence zone areas with a different probability content (90%, 95%, and 99%).

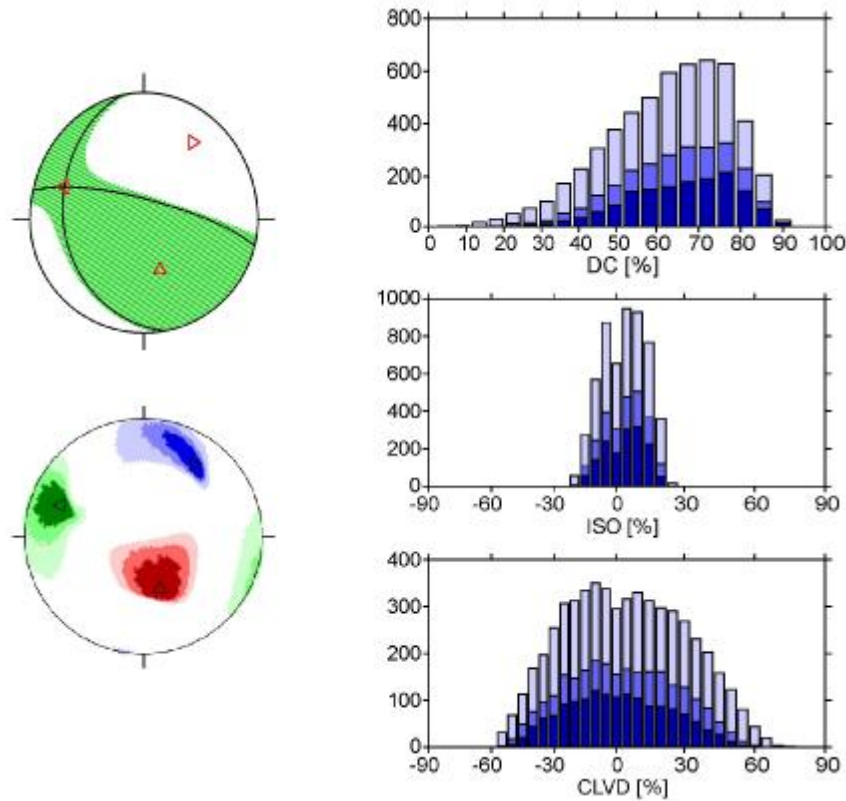


Figure 16: The source mechanism for the actual event on March 5, 2012 retrieved using a general moment tensor. The traditional fault-plane solution and the principal T, P, and N axes are displayed together with the histograms of the individual components of the decomposed MT (DC, V, and CLVD). Different colors represent the confidence zones of different probabilities. Dark, medium, and light colors correspond, in turn, to probabilities of 90%, 95%, and 99%.

The confidence zones of the principal T, P, and N axes were well constrained such that the orientation of the double-couple part of the mechanism was likely correctly retrieved. However, the DC histogram was wide, indicating uncertain determination for the shear-slip component. The V histogram was quite narrow and symmetrical around a

value of zero, suggesting a mechanism without volumetric changes. On the contrary, the CLVD histogram was very wide which could be a result of noise contamination, as demonstrated in previous synthetic tests. The confidence intervals of both the V and CLVD components included a value of zero, indicating that pure shear could well be the actual solution.

4. Conclusions

The data quality and the accuracy of the velocity model for an area of interest are very important for moment tensor inversions. The velocity data available for the Dobrá Voda area enabled the construction of both 1-D and 3-D smooth structural velocity models. The models were suitable for ray tracing and enabled us to calculate the response of the medium, which was then used for MT inversion. The 3-D model realistically described basic structural features of the locality.

We performed a synthetic case study by simulating seismic observations for the Dobrá Voda area in order to demonstrate the effects of using a 1-D approximation of the structure or an exact 3-D structural model during the MT inversion. In the 3-D model, we generated synthetic P- and S-wave amplitudes which were then altered by artificial random white noise with maximum amplitude equal to 10 and 20% of the maximum amplitude within the dataset. A total of 100 datasets were generated for each level of noise. We then inverted the data using both the 3-D and 1-D models. We found that using the inexact velocity model generates more spurious non-DC components within the mechanism. This fact should be taken into account during the interpretation. Using the exact 3-D model enabled to use less data or data of lower quality for the MT inversion and to still obtain reasonable results. Nevertheless, the double-couple component appeared to be sufficiently accurate to properly identify the fault plane orientation, even from noisy data, with a simple structural model. If a complete reading of P- and S-wave amplitudes of high quality is available, a coarse structural model (even 1-D) may be sufficient.

Source mechanisms of five strong events observed over the last few years were retrieved using an unconstrained moment tensor and pure DC inversions of the peak amplitudes of direct P- and S-waves extracted from seismograms of the MKNET network. Using the 3-D laterally inhomogeneous model in the MT inversion provided smaller non-DC components of the mechanisms as compared to the 1-D model. Retrieved mechanisms of the events indicated that all five microearthquakes were nearly pure shear-slips.

Acknowledgements

We thank two anonymous reviewers for comments that helped us improve the manuscript. Seismic data were provided by ProgSeis. We are indebted to Juraj Sekereš for careful preparation of the MKNET data, and the precise location of seismic events. We are grateful to Jan Šílený and Luděk Klimeš for advice and comments.

Our research was supported by the Grant Agency of the Czech Republic under Contracts P210/10/1728 and P210/10/0736, by the Ministry of Education of the Czech Republic within Research Project MSM0021620860, by the European Community's FP7 Consortium Project AIM (Advanced Industrial Microseismic Monitoring), Grant Agreement No. 230669, and by members of the "Seismic Waves in Complex 3-D Structures" consortium (see "<http://sw3d.cz>").

References

- Aki, K., and Richards, P.G., 1980, *Quantitative seismology: theory and methods*, W.H. Freeman, San Francisco, USA, 932 pp.
- Bouchon, M., 2003, A review of the discrete wavenumber method, *Pure Appl. Geophys.* **160**, 445–465.
- Bulant, P., 2002, Sobolev scalar products in the construction of velocity models - application to model Hess and to SEG/EAGE Salt Model, *Pure Appl. Geophys.* **159**, 1487-1506.
- Bulant, P., 2004, Constructing the SEG/EAGE 3-D Salt Model for ray tracing using Sobolev scalar products, *Stud. geophys. geod.* **48**, 689-707.
- Coutant, O., 1990, Program of numerical simulation AXITRA, *Laboratoire de Géophysique Interne et Tectonophysique Report*, University of Joseph Fourier (in French).
- Červený, V., Klimeš, L., and Pšenčík, I., 1988, Complete seismic-ray tracing in three-dimensional structures. In: Doornbos, D.J. (ed.), *Seismological Algorithms*, pp. 89-168, Academic Press, New York.
- Fojtíková, L., Vavryčuk, V., Cipciar, A., and Madarás, J., 2010, Focal mechanisms of micro-earthquakes in the Dobrá Voda seismoactive area in the Malé Karpaty Mts. (Little Carpathians), Slovakia, *Tectonophysics* **492**, 213–229, doi:10.1016/j.tecto.2010.06.007.
- Geofyzika Brno, 1985, Velocity model JAB90_3D_B.MOD.
- Godano, M., Bardainne, T., Regnier, M., and Deschamps, A., 2011, Moment-tensor determination by nonlinear inversion of amplitudes, *Bull. Seism. Soc. Am.*, **101** (1), 366-378, doi:10.1785/0120090380.
- Hók, J., Vojtko, R., and Fojtíková, L., 2009, Geological-tectonic scheme of pre-Tertiary bedrock south-west segment of Carpathian Mountains, unpublished.
- Hudson, J.A., Pearce, R.G., and Rogers, R.M., 1989, Source type plot for inversion of the moment tensor, *J. Geophys. Res.* **94**, 765-774, doi:10.1029/JB094iB01p00765.
- Jechumtálová, Z., and Šílený, J., 2005. Amplitude ratios for complete moment tensor retrieval, *Geophys. Res. Lett.* **32**, L22303, doi:10.1029/2005GL023967.
- Jechumtálová, Z., Šílený, J., and Trifu, C. 2014. Microearthquake mechanism from wave amplitudes recorded by a close-to-surface seismic array at Ocele Mari, Romania, *Geophys. J. Int.*, doi: 10.1093/gji/ggu029.
- Káčer, Š., Antalík, M., Lexa, J., Zvara, I., Fritzman, R., Vlachovič, J., Bystrická, G., Brodianska, M., Potfaj, M., Madarás, J., Nagy, A., Maglay, J., Ivanička, J., Gross, P., Rakús, M., Vozárová, A., Buček, S., Boorová, D., Šimon, L., Mello, J., Polák, M., Bezák, V., Hók, J., Tet'ák, F., Konečný, V., Kučera, M., Žec, B., Elečko, M., Hraško, L., Kováčik, M., and Pristáš, J., 2005, Slovak Republic – digital geological map 1:50 000 and 1:500 000. Final report. Geofond, Bratislava (in Slovak).
- Kárník, V., 1968. Seismicity of the European Area. Part 1. *Academia*, Praha.
- Kárník, V., 1971. Seismicity of the European Area. Part 2. *Academia*, Praha.
- Kolář, P., 2007, Interactive seismic viewer "OP" - Short review, *Acta Geodyn. Geomater.* **4**, 21-25.
- Mahel', M., 1986, Geologická stavba československých Karpát: díl 1: Paleoalpínské jednotky, *Veda, Vydavateľstvo Slovenskej akadémie vied Geologický ústav Dionýza*

Štúra, 503 pp.

- Marko, F., Fodor, L., and Kováč, M., 1991, Miocene strike-slip faulting and block rotation in Brezovské Karpaty Mts. (Western Carpathians), *Mineralia Slovaca* **23**, 189–200.
- Press, W.H., Teukolsky, S.A., Vetterling, W.T., and Flannery, B.P., 1992, Numerical Recipes, *Cambridge University Press*.
- Rössler, D., Rumpker, G., and Krüger, F., 2004, Ambiguous moment tensors and radiation patterns in anisotropic media with applications to the modelling of earthquake mechanisms in W-Bohemia, *Stud. Geophys. Geod.*, **48**, 233–250.
- Sokos, E., and Zahradník, J., 2009, ISOLA—A Fortran code and Matlab GUI to perform multiplepoint source inversion of seismic data, *Comput. Geosci.* **34**, 967–977.
- Snoke, J. A., 2003, FOCMEC: FOCal MECHANISM determinations, in *International Handbook of Earthquake and Engineering Seismology*, edited by W. H. K. Lee et al., chap. 85.12, pp. 29–30, Elsevier, New York.
- Šílený, J., Panza, G. F., and Campus, P., 1992, Waveform inversion for point source moment tensor retrieval with variable hypocentral depth and structural model, *Geophys. J. Int.* **109**, 259–274.
- Šílený, J., Campus, P., and Panza, G. F., 1996, Earthquake mechanism resolution by waveform inversion of a few local noisy records – I. Synthetic tests, *Geophys. J. Int.* **126**, 605–619.
- Šílený, J., and Vavryčuk, V., 2002, Can unbiased source be retrieved from anisotropic waveforms by using an isotropic model of the medium? *Tectonophysics*, **356**, 125–138.
- Šílený, J., and Milev, A., 2008, Source mechanism of mining induced seismic events - Resolution of double couple and non double couple models, *Tectonophysics* **456**, 3–15, doi:10.1016/j.tecto.2006.09.021.
- Šílený, J., 2009, Resolution of non-double-couple mechanisms: Simulation of hypocenter mislocation and velocity structure mismodeling, *Bull. Seism. Soc. Am.* **99** (4), 2265–2272, doi:10.1785/0120080335.
- Šílený, J., Jechumtálová, Z., and Dorbath, C., 2014, Small scale earthquake mechanisms induced by fluid injection at the Enhanced Geothermal System reservoir Soultz (Alsace) in 2003 using alternative source models, *Pure Appl. Geophys.*, doi: 10.1007/s00024-013-0750-2.
- Tarantola, A. (1987). Inverse Problem Theory. Methods for Data Fitting and Model Parameter Estimation, *Elsevier*.
- Vavryčuk, V., 2001, Inversion for parameters of tensile earthquakes, *J. Geophys. Res.* **106** (B8), 16339–16355.
- Vavryčuk, V., 2009, The amplitude moment tensor inversion — program AMT, Computer codes library, Institute of Geophysics, Prague.
- Žáček, K., 2002, Smoothing the Marmousi model, *Pure Appl. Geophys.* **159**, 1507–1526.